High-resolution extended source optical coherence tomography

Yu, Xiaojun; Liu, Xinyu; Chen, Si; Luo, Yuemei; Wang, Xianghong; Liu, Linbo

2015

Yu, X., Liu, X., Chen, S., Luo, Y., Wang, X., & Liu, L. (2015). High-resolution extended source optical coherence tomography. Optics Express, 23(20), 26399-26413.

https://hdl.handle.net/10356/81673

https://doi.org/10.1364/OE.23.026399

High-resolution extended source optical coherence tomography

Xiaojun Yu,[1,*] Xinyu Liu,[1] Si Chen,[1] Yuemei Luo,[1] Xianghong Wang,[1] and Linbo Liu[1,2,*]

[1]*School of Electrical & Electronic Engineering, Nanyang Technological University, Singapore*

[2]*School of Chemical and Biomedical Engineering, Nanyang Technological University, Singapore*

[*]*LIULINBO@ntu.edu.sg*

Abstract: High resolution optical coherence tomography (OCT) is capable of providing detailed tissue microstructures that are critical for disease diagnosis, yet its sensitivity is usually degraded since the system key components are typically not working at their respective center wavelengths. We developed a novel imaging system that achieves enhanced sensitivity without axial resolution degradation by the use of a spectrally encoded extended source (SEES) technique; it allows larger sample power without exceeding the maximum permissible exposure (MPE). In this study, we demonstrate a high-resolution extended source (HRES) OCT system, which is capable of providing a transverse resolution of 4.4 μm and an axial resolution of 2.1 μm in air with the SEES technique. We first theoretically show a sensitivity advantage of 6-dB of the HRES-OCT over that of its point source counterpart using numerical simulations, and then experimentally validate the applicability of the SEES technique to high-resolution OCT (HR-OCT) by comparing the HRES-OCT with an equivalent point-source system. In the HRES-OCT system, a dispersive prism was placed in the infinity space of the sample arm optics to spectrally extend the visual angle (angular subtense) of the light source to 10.3 mrad. This extended source allowed ~4 times larger MPE than its point source counterpart, which results in an enhancement of ~6 dB in sensitivity. Specifically, to solve the unbalanced dispersion between the sample and the reference arm optics, we proposed easy and efficient methods for system calibration and dispersion correction, respectively. With a maximum scanning speed reaching up to 60K A-lines/s, we further conducted imaging experiments with HRES-OCT using the human fingertip *in vivo* and the swine eye tissues *ex vivo*. Results demonstrate that the HRES-OCT is able to achieve significantly larger penetration depth than its conventional point source OCT counterpart.

OCIS codes: (110.4500) Optical coherence tomography; (170.4500) Optical coherence tomography; (170.3890) Medical optics instrumentation; (170.3880) Medical and biological imaging; (170.4470); Ophthalmology (170.4470).

References and links

1. D. Huang, E. A. Swanson, C. P. Lin, J. S. Schuman, W. G. Stinson, W. Chang, M. R. Hee, T. Flotte, K. Gregory, C. A. Puliafito, and J. G. Fujimoto, "Optical coherence tomography," Science **254**, 1178-1181 (1991).
2. A. F. Fercher, C. K. Hitzenberger, G. Kamp, and S. Y. El-Zaiat, "Measurement of intraocular distances by backscattering spectral interferometry," Opt. Commun. **117**, 43-48 (1995).
3. W. Drexler and J. G. Fujimoto, *Optical Coherence Tomography: Technology and Applications* (Springer, 2008).
4. B. Cense, N. Nassif, T. Chen, M. Pierce, S.-H. Yun, B. Park, B. Bouma, G. Tearney, and J. de Boer, "Ultrahigh-resolution high-speed retinal imaging using spectral-domain optical coherence tomography," Opt. Express **12**, 2435-2447 (2004).
5. W. Drexler and J. G. Fujimoto, "State-of-the-art retinal optical coherence tomography," Prog. Retin. Eye Res **27**, 45-88 (2008).

6. I. Grulkowski, J. J. Liu, B. Potsaid, V. Jayaraman, C. D. Lu, J. Jiang, A. E. Cable, J. S. Duker, and J. G. Fujimoto, "Retinal, anterior segment and full eye imaging using ultrahigh speed swept source OCT with vertical-cavity surface emitting lasers," Biomed. Opt. Express **3**, 2733-2751 (2012).
7. Y. Hori, Y. Yasuno, S. Sakai, M. Matsumoto, T. Sugawara, V. Madjarova, M. Yamanari, S. Makita, T. Yasui, and T. Araki, "Automatic characterization and segmentation of human skin using three-dimensional optical coherence tomography," Opt. Express **14**, 1862-1877 (2006).
8. M. Mogensen, T. JOERGENSEN, B. M. Nürnberg, H. A. Morsy, J. B. THOMSEN, L. Thrane, and G. B. Jemec, "Assessment of optical coherence tomography imaging in the diagnosis of non‐melanoma skin cancer and benign lesions versus normal skin: observer‐blinded evaluation by dermatologists and pathologists," Dermatol. Surg. **35**, 965-972 (2009).
9. T. Gambichler, P. Regeniter, F. G. Bechara, A. Orlikov, R. Vasa, G. Moussa, M. Stücker, P. Altmeyer, and K. Hoffmann, "Characterization of benign and malignant melanocytic skin lesions using optical coherence tomography in vivo," J. Am. Acad. Dermatol. **57**, 629-637 (2007).
10. G. Tearney, M. Brezinski, J. Southern, B. Bouma, S. Boppart, and J. Fujimoto, "Optical biopsy in human gastrointestinal tissue using optical coherence tomography," Am. J. Gastroenterol. **92**, 1800-1804 (1997).
11. A. R. Tumlinson, B. Považay, L. P. Hariri, J. McNally, A. Unterhuber, J. K. Barton, B. Hermann, H. Sattmann, and W. Drexler, "In vivo ultrahigh-resolution optical coherence tomography of mouse colon with an achromatized endoscope," J. Biomed. Opt. **11**, 064003-064003-064008 (2006).
12. O. O. Ahsen, H.-C. Lee, K. Liang, M. G. Giacomelli, T.-H. Tsai, Z. Wang, M. Figueiredo, Q. Huang, B. Potsaid, and J. G. Fujimoto, "Ultrahigh speed optical coherence tomography with micromotor imaging probe enables three-dimensional visualization of mucosal surface patterns in the gastrointestinal tract," Gastroenterology **5**, S-519 (2014).
13. M. E. Brezinski, G. J. Tearney, B. E. Bouma, S. A. Boppart, M. R. Hee, E. A. Swanson, J. F. Southern, and J. G. Fujimoto, "Imaging of coronary artery microstructure (in vitro) with optical coherence tomography," Am. J. Cardiol. **77**, 92-93 (1996).
14. T. Kume, T. Akasaka, T. Kawamoto, Y. Ogasawara, N. Watanabe, E. Toyota, Y. Neishi, R. Sukmawan, Y. Sadahira, and K. Yoshida, "Assessment of coronary arterial thrombus by optical coherence tomography," Am J Cardiol **97**, 1713-1717 (2006).
15. L. Liu, J. A. Gardecki, S. K. Nadkarni, J. D. Toussaint, Y. Yagi, B. E. Bouma, and G. J. Tearney, "Imaging the subcellular structure of human coronary atherosclerosis using micro-optical coherence tomography," Nat. Med. **17**, 1010-1014 (2011).
16. N. Hanna, D. Saltzman, D. Mukai, Z. Chen, S. Sasse, J. Milliken, S. Guo, W. Jung, H. Colt, and M. Brenner, "Two-dimensional and 3-dimensional optical coherence tomographic imaging of the airway, lung, and pleura," J. Thorac. Cardiovasc. Surg. **129**, 615-622 (2005).
17. B. C. Quirk, R. A. McLaughlin, A. Curatolo, R. W. Kirk, P. B. Noble, and D. D. Sampson, "In situ imaging of lung alveoli with an optical coherence tomography needle probe," J. Biomed. Opt. **16**, 036009-036009-036004 (2011).
18. S. Lam, B. Standish, C. Baldwin, A. McWilliams, A. Gazdar, A. I. Vitkin, V. Yang, N. Ikeda, and C. MacAulay, "In vivo optical coherence tomography imaging of preinvasive bronchial lesions," Clin. Cancer Res. **14**, 2006-2011 (2008).
19. R. Leitgeb, W. Drexler, A. Unterhuber, B. Hermann, T. Bajraszewski, T. Le, A. Stingl, and A. Fercher, "Ultrahigh resolution Fourier domain optical coherence tomography," Opt. Express **12**, 2156-2165 (2004).
20. M. Wojtkowski, V. J. Srinivasan, T. H. Ko, J. G. Fujimoto, A. Kowalczyk, and J. S. Duker, "Ultrahigh-resolution, high-speed, Fourier domain optical coherence tomography and methods for dispersion compensation," Opt. Express **12**, 2404-2422 (2004).
21. W. Drexler, "Ultrahigh-resolution optical coherence tomography," J. Biomed. Opt. **9**, 47-74 (2004).
22. N. Nassif, B. Cense, B. Park, M. Pierce, S. Yun, B. Bouma, G. Tearney, T. Chen, and J. de Boer, "In vivo high-resolution video-rate spectral-domain optical coherence tomography of the human retina and optic nerve," Opt. Express **12**, 367-376 (2004).
23. B. Cense, T. C. Chen, B. H. Park, M. C. Pierce, and J. F. de Boer, "In vivo birefringence and thickness measurements of the human retinal nerve fiber layer using polarization-sensitive optical coherence tomography," J. Biomed. Opt. **9**, 121-125 (2004).
24. F. C. Delori, R. H. Webb, and D. H. Sliney, "Maximum permissible exposures for ocular safety (ANSI 2000), with emphasis on ophthalmic devices," J. Opt. Soc. Am. A **24**, 1250-1265 (2007).
25. T. Bonin, G. Franke, M. Hagen-Eggert, P. Koch, and G. Hüttmann, "In vivo Fourier-domain full-field OCT of the human retina with 1.5 million A-lines/s," Opt. Lett. **35**, 3432-3434 (2010).
26. B. Grajciar, M. Pircher, A. Fercher, and R. Leitgeb, "Parallel Fourier domain optical coherence tomography for in vivo measurement of the human eye," Opt. Express **13**, 1131-1137 (2005).
27. Y. Nakamura, S. Makita, M. Yamanari, M. Itoh, T. Yatagai, and Y. Yasuno, "High-speed three-dimensional human retinal imaging by line-field spectral domain optical coherence tomography," Opt. Express **15**, 7103-7116 (2007).
28. D. J. Fechtig, B. Grajciar, T. Schmoll, C. Blatter, R. M. Werkmeister, W. Drexler, and R. A. Leitgeb, "Line-field parallel swept source MHz OCT for structural and functional retinal imaging," Biomedical Opt. Express **6**, 716-735 (2015).

29. D. J. Fechtig, T. Schmoll, B. Grajciar, W. Drexler, and R. A. Leitgeb, "Line-field parallel swept source interferometric imaging at up to 1 MHz," Opt. Lett. **39**, 5333-5336 (2014).
30. X. Liu, X. Yu, H. Tang, D. Cui, M. R. Beotra, M. J. Girard, D. Sun, J. Gu, and L. Liu, "Spectrally encoded extended source optical coherence tomography," Opt. Lett. **39**, 6803-6806 (2014).
31. I. E. Commission, "IEC 60825-1," Safety of Laser Products—Part **1**(2001).
32. S. Yun, G. Tearney, B. Bouma, B. Park, and J. de Boer, "High-speed spectral-domain optical coherence tomography at 1.3 μm wavelength," Opt. Express **11**, 3598-3604 (2003).
33. B. Park, M. C. Pierce, B. Cense, S.-H. Yun, M. Mujat, G. Tearney, B. Bouma, and J. de Boer, "Real-time fiber-based multi-functional spectral-domain optical coherence tomography at 1.3 μm," Opt. Express **13**, 3931-3944 (2005).

1. Introduction

Optical coherence tomography is a low coherence interferometry based imaging technology that provides cross-sectional images of the biological tissues and materials [1-3]. Due to its high-resolution and non-invasive properties, OCT has attracted much attention in the past two decades, and now has been established as a routine clinical imaging tool for the diagnosis of both eye and skin diseases [4-9]. In OCT, the axial (depth) and transverse resolutions are decoupled: the transverse resolution is determined by the diffraction limited spot size of the focused beam, while the axial resolution is decided by the center wavelength and bandwidth of the light source. The typical spatial resolution of the current ophthalmic OCT devices is around 5-10 μm (in air) in the axial direction and is around 15 μm in the transverse direction. So far, extensive efforts have been made to improve OCT spatial resolutions to obtain clearer images of the biological tissue microstructures, such as the retinal layers [4-6], the skin lesions [7-9], the gastrointestinal tissues [10-12], the coronary artery structures [13-15], and the pulmonary bronchus [16-18], etc., *in vivo* and *ex vivo*.

In order to improve the axial resolution, light sources with a broader bandwidth are introduced [4, 19-21]. Usually, the broadband spectral responses of most of the key components are reduced with respect to their spectral responses within the relative narrow band around the center wavelength. This reduction in spectral responses inevitably leads to imaging sensitivity degradation with respect to the standard resolution (~10 um) devices. For example, the reduced spectral responses of the linear camera, the dispersion grating, and the focusing lenses (chromatic focal shift) may amount up to a total sensitivity disadvantage of several dBs [15, 21, 22]. Such sensitivity disadvantage may limit the applications of this class of techniques.

A straightforward solution to compensate the signal loss is to increase the optical power on the sample. However, the maximum permissible radiant exposure level to the human eye and the skin is limited according to the laser safety regulations [23, 24], which consequently limits the sensitivity of the current high-resolution OCT (HR-OCT) technologies, especially for ophthalmic and skin imaging. A limited sensitivity usually impedes our ability to acquire the high quality OCT images, due to the insufficient penetration depth and imaging speed.

The sensitivity loss in HR-OCT may be compensated by the use of an extended source illumination, which potentially allows larger maximum permissible exposure (MPE) than that of the point source. Extended source illumination can be realized either with an extended field scheme (full-field OCT) [25] or a line focus scheme (line-field OCT) [26-30]. Different OCT systems with such schemes have been demonstrated. Utilizing a frequency swept source and an ultrafast CMOS camera for spatially parallel image acquisition, Bonin *et al*. demonstrated a parallel full field OCT with maximum acquisition speed of 1.5 MA-scans/s for retinal imaging [25]. The spectrometer based line-field OCT (SLF-OCT), which records a full B-scan spectral interference spectra in parallel with a single shot, was also demonstrated [26, 27]. The first SLF-OCT for 2-dimentional (2D) biological tissue imaging *in vivo* achieved an acquisition speed of 256 kHz with a sensitivity of 89 dB [26]. Later, with the same line-field scheme adopted for 3D retinal imaging *in vivo*, Nakamura *et al.* demonstrated an acquisition speed of

51 kHz at a detection sensitivity of 89.4 dB in [27]. To reduce the influences of spectral and spatial crosstalk from the scattering object, the line-field parallel swept source interferometric imaging (LPSI) scheme was reported recently [28, 29]. By combing line-field swept source OCT with the modulation of the interferometric signal in the spatial direction for full range imaging, LPSI achieved an acquisition speed of up to 1 MHz equivalent A-scan rate with a sensitivity better than 93.5 dB. More recently, Liu *et al.* demonstrated a spectrally encoded extended source (SEES) technique to allow larger sample power for ophthalmic imaging [30]. Using a dispersive element to spread the radiation spectrum of the small source into a linear source, SEES technique improved the imaging sensitivity by ~5 dB comparing with its point-source counterpart. However, all those demonstrated systems are of standard resolutions, and no previous work, to the best of our knowledge, has ever been done to improve the sensitivity of HR-OCT systems. With the increasing popularity and wide clinical applications of HR-OCT in recent years, sensitivity enhancement now becomes a critical issue for high-resolution OCT imaging.

In this paper, we demonstrate the feasibility of HR-OCT imaging with sensitivity enhancement using the SEES technique. We first calculated the sensitivity advantage of SEES based HR-OCT relative to the corresponding point source system. We secondly developed a high-resolution extended source (HRES) OCT system, which achieved a transverse resolution of 4.4 μm and an axial resolution of 2.1 μm in air. We finally imaged the human fingertip *in vivo* and the swine eye tissues *ex vivo* to demonstrate the advantage of HRES-OCT system over a typical point source OCT system in achieving higher penetration depth.

2. Methods

2.1 Working principle

A schematic diagram of the SEES based OCT system is shown in Fig. 1. The SEES technique relies on a dispersive element (a prism was utilized in this study) to spread the light radiation spectrum such that the sample light is transformed into a linear source. Unlike the most existing SD-OCT systems which employ point sources with the angular subtense $\alpha < 1.5$ mrad, the SEES based OCT produces a linear source with the angular subtense $\alpha > 1.5$ mrad, such that the transformed source qualifies for an extended source according to the laser safety regulations, e.g., IEC 60825-1 [31]. The MPE value for a non-circular source can be improved by a factor of C_6 as indicated in Eq. (1). C_6 is proportional to the arithmetic mean of the horizontal and vertical angular of the source,

$$MPE_{ext} = C_6 \times MPE_{point\ source} = \frac{(\alpha + \alpha_{\min})}{2\alpha_{\min}} \times MPE_{point\ source} \quad (1)$$

wherein $\alpha_{min} = 1.5$ mrad is the minimum angular subtense while α is the actual angular subtense.

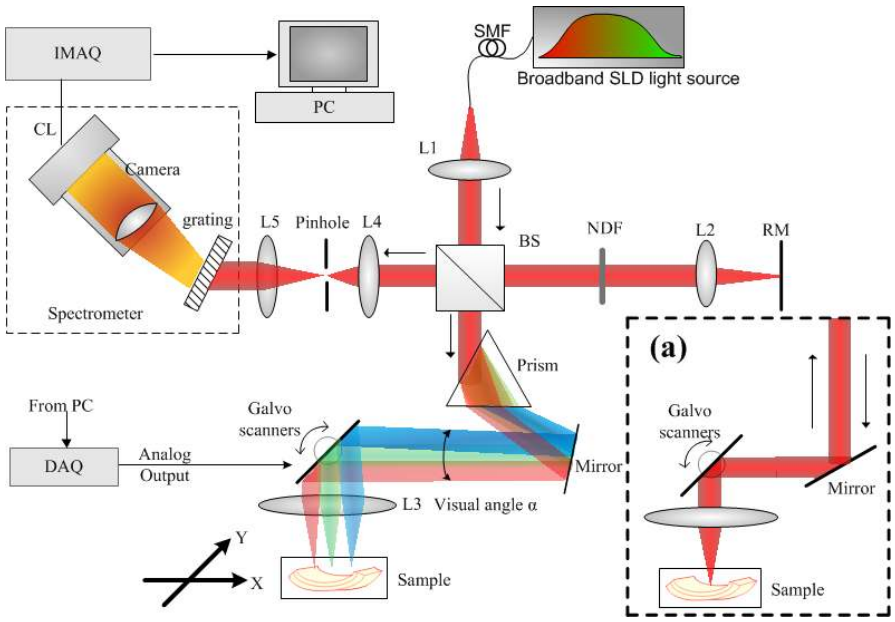

Fig. 1. Experimental setup of the HRES-OCT system. (a) The sample arm optics of a standard point source SD-OCT built for comparison purpose. SLD: super luminescent diode; SMF: signal mode fiber; BS: non-polarizing beam splitter; NDF: Neutral density filter; IMAQ: image acquisition board; CL: Camera Link cable; DAQ: data acquisition card; PC: personal computer; RM: reference mirror; L1-5: achromatic lens.

Numerical simulations were conducted to demonstrate the MPE and the potential sensitivity enhancement effects with the SEES technique. Assume that a light source with a center wavelength of λ_c = 850 nm and a bandwidth of $\Delta\lambda$ = 165 nm at the full-width at half-maximum (FWHM) was adopted in such an OCT system. If a dispersive F2 prism was utilized at the sample arm optics to achieve an angular subtense of α = 10.3 mrad, then the MPE value of this OCT was C_6 = 3.93 times higher than that of its point source counterpart according to Eq. (1).

The following signal to noise ratio (SNR) formula [32] were utilized for theoretical analysis of the system sensitivity,

$$S[\mathrm{dB}] = 10 \times \log\left(\frac{N_{ref} \sum N_S}{N_{sh}^2 + N_{el}^2 + N_{RIN}^2} \right) \tag{2}$$

$$N_{sh} = N_{ref}^{1/2} \tag{3}$$

$$N_{RIN} = \left(f / \Delta\nu \right)^{1/2} N_{ref} \tag{4}$$

wherein N_{ref} is the number of electrons per pixel generated by the reference arm light, N_{sh} is the number of shot noise electrons, N_{el} is the electrical noise of the photodetector, N_{RIN} is the relative intensity noise, f is the reciprocal of twice the exposure time of CCD, $\Delta\nu$ is the FWHM spectral bandwidth of the reference light received by a single pixel, and $\sum N_s$ is the sum of electrons over the entire array generated by the sample arm light reflected back by a 100% reflector.

We further assumed that an E2v AVIIVA EM4 BA9 camera with a full well depth of 0.3125 Me^- for each pixel was utilized for spectral data detection; the spectrometer and the grating efficiencies were 0.5 and 0.7, respectively. The exposure time was set to be 97.7 μs, hence, the theoretical sensitivity as a function of the reference reflectivity for an OCT system with/without SEES technique is depicted in Fig. 2. The illumination power on the sample was

set to be 4.8 mW for SEES-OCT and 1.2 mW for point source system, respectively. As can be seen, the maximum theoretical sensitivity was achieved at the camera saturation level for both systems. With the SEES scheme (Fig. 2(a)), the sensitivity was ~6 dB higher than that of the system without SEES (Fig. 2(b)). Specifically, the theoretical sensitivity of the SEES based OCT system was calculated to be 106.3 dB with N_{ref} = 386.53 Me^- and N_{sh} = 19,660 e^-, while RIN noise N_{rin}, electrical noise N_{el} as well as $\sum N_s$ were calculated to be 3,325 e^-, 587 e^- and 4.375×10^{10} e^- according to Eqs. (3-4).

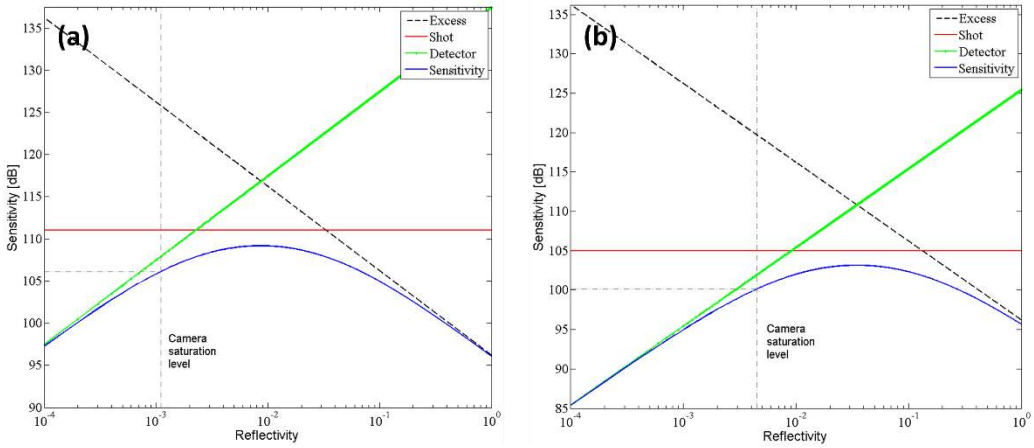

Fig. 2. Theoretical sensitivity of the OCT system as a function of reference reflectivity. (a) The OCT system with the SEES technique. (b) The point-source system without the SEES technique.

2.2 Experimental setup

We applied the SEES technique to a high-resolution OCT system to experimentally verify its feasibility for sensitivity enhancement. Figure 1 shows the experimental setup of the HRES-OCT system. A super luminescent diode (SLD) array (Superlum Broadlighters T-850-HP) with a center wavelength of λ_c = 850 nm and a FWHM bandwidth of $\Delta\lambda$ = 165 nm was employed as the light source of the OCT system. The output power was measured to be 17.9 mW. The generated light was collimated by a lens L1 (AC050-010-B-ML, Thorlabs Inc.) and then was split into two separate beams by a 50:50 non-polarizing beam splitter (BS: BS005, Thorlabs Inc.). The reference light transmitted through a neutral density filter (NDF: NDL-10C-4) and was focused by a lens L2 (AC080-016-B-ML, Thorlabs Inc.). Finally, it was backward reflected by the reference mirror (RM).

The collimated beam of the sample arm was transformed into a dispersive fan beam with a visual angular range of 10.3 mrad after transmitting through an equilateral prism (PS856, Thorlabs Inc.). The fan beam was then coupled into a pair of galvo scanners (GVSM002/M, Thorlabs Inc.), and focused on to the sample by an objective lens L3 (AC080-016-B-ML, Thorlabs Inc.). The light power illuminating the sample was measured to be 4.79 mW; the full-length at half-maximum of the illumination line on the sample plane was calculated to be 164.8 µm.

The light backreflected from the reference arm and backscattered from the sample arm was recombined to generate interferometric signals after passing through the 50:50 beam splitter. These signals were filtered by a spatial filter and then collected by a spectrometer system. The spatial filter consisted of an achromat lens L4 (AC050-010-B-ML, Thorlabs Inc.), a 10 µm pinhole (P10S, Thorlabs Inc.) and another achromat lens L5 (AC127-030-B, Thorlabs Inc.); the spectrometer consisted of a diffraction grating (1200 l/mm @ 830nm, Wasatch Photonics Inc.), a camera lens (Nikon AF Nikkor 85mm f/1.8D), and a line scan camera (E2V, AViiVA

EM4). Taking the grating diffraction efficiency, sensor quantum efficiency, and camera lens efficiency into account, the spectrometer efficiency was measured to be 0.456. The detected signal was digitized at a 12-bit digital resolution, and then was transferred to a computer through two camera link cables and an image acquisition card (KBN-PCE-CL4-F, Bitflow Inc.). Both of the camera and galvo scanners were synchronized by a triggering signal generated by the computer. The line rate and the exposure time of the camera were set to be 10 kHz and 97.7 μs, respectively. The number of camera pixels was measured to be 1335 at FWHM. The scanning direction (X) of the fast galvo scanner was aligned along the illumination line and the slow galvo direction (Y) perpendicular to the illumination line [30].

2.3 System calibration

Each camera pixel detected a single narrow spectral band of the light source. As the fast galvo scanner scanned the illumination line through a given sample point, the light signals of different spectral bands arrived at this point sequentially in time; the arrival time of a spectral band relative to that of the first spectral band is decided by the dispersive property of the prism as well as the galvo scanner's scanning speed. In another word, the light signals of different spectral bands backscattered from the same sample point spread over multiple sequential camera acquisitions. In order to align all the spectral bands from each sample point into the same spectral line, we need to shift the A-line sequence number of each spectral band according to its arrival time. To do so, we adopted a simple and efficient cross-correlation mechanism. The basic idea of such a mechanism was to find the time delay n (in A-line sequence number) for the light signal received by a camera pixel, respect to the arrival time of that of a reference pixel. Assuming the A-line sequence number of the pixel was N, by shifting the A-line sequence number back to N-n, all the light signals backscattered from the same sample point were aligned with the same A-line sequence number. Assume that $s[p]$ was the reference spectrum data sequence s that was detected by the camera pixel p, and $y[m]$ was another spectrum data sequence y received by the camera pixel m, then the calibration mechanism can be expressed as follows,

$$n = \arg\max_{m} \left(s(p) * y(m) \right) \tag{5}$$

Once the time delay n is found for $y[m]$, such spectrum data sequence then can be shifted by a time delay n to align with $s[p]$.

To conduct the spectral remapping, we placed a United States Air Force (USAF) 1951 resolution target (#57-896, Edmund Optics Inc.) at the focal plane, and acquired a B-scan frame of the chromium-coated line pattern on the target with the reference arm blocked. Fig. 3(a) presents an acquired B-scan frame consisting of 512 consecutive spectral lines. It is worth noting that, since the illumination light spectrum cannot cover all the 2048 spectrometer pixels, the data that was collected by the camera pixels from 1 to 165 and from 1971 to 2048 was omitted in the calibration process (dark area outside the two horizontal yellow lines in Fig. 3(a)). In the experiments, the spectrum data sequence that was acquired by the camera pixel p=1000 (red arrow in Fig. 3(a)) was chosen as the reference spectrum data sequence $s[p]$.

After the cross-correlation calculation for the spectrum data sequence collected by each effective camera pixel, the discrete time delay n (in A-line sequence number) for each camera pixel was obtained as shown by the red-dashed-line with circle markers in Fig. 3(b). In order to remap all the spectrum data sequences, a continuous look-up table has to be obtained. Hence, the discrete time delay data was further fitted to a 10-order polynomial function to obtain the continuous remapping curve (solid-blue-line in Fig. 3(b)). With such continuous look-up table, the B-scan frame was remapped so that the spectrum of every point on the sample was aligned to a vertical A-scan line, as shown in Fig. 3(c). It is also worth mentioning that the B-scan range was set to be 0.98 mm in the experiments. As a result, a scan margin of

112 A-lines was introduced (black area at the right corner in Fig. 3(c)), and therefore, the effective scan range was smaller than the actual range.

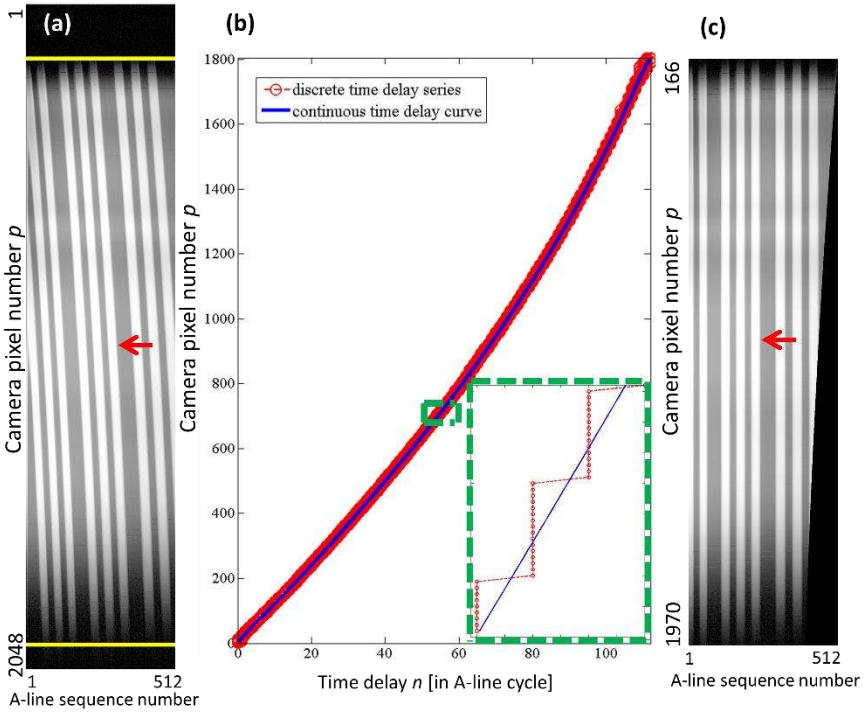

Fig. 3. Calibration process for HRES-OCT. (a) The B-scan frame consisting of 512 consecutive spectral lines was acquired for system calibration. The spectrum data that was detected by camera pixels from 166 to 1970 within two horizontal yellow lines was used for calibration. (b) The obtained time-delay series corresponding to each of the effective camera pixel. Red-dashed-line with circle markers: the discrete time delay series; solid-blue-line: the obtained continuous curve that was used as a look-up table for spectral remapping. (c) The acquired B-scan frame after spectral remapping.

2.4 Dispersion compensation

With the prism inserted into the sample arm optics, the dispersion between the reference and sample arms is mismatched, which thus causes distortions to the OCT images. To deal with this issue, we developed a novel and efficient algorithm for dispersion compensation. The main idea of such an algorithm is based on the fact that when using a reflector as the sample, an SD-OCT should produce a perfect sinusoidal interferogram in *k*-space.

As aforementioned, since there exist the dispersion mismatch issue as well as the *k*-space nonlinearity problem, the interferograms obtained in the experiments were not perfectly sinusoidal but a 'chirped' sinusoidal function. Hence, if we find a look-up vector that is able to remap the 'chirped' interferogram back to a perfect sinusoidal interferogram, both the dispersion mismatch and the *k*-space nonlinearity issues can be solved. The proposed mechanism has two main steps: the first step is to accurately remap the interferogram from CCD detector index space to *k*-space, and the second step is to compensate the dispersion between the reference and sample arm optics. The theoretical modeling of this method was described as follows.

Assume *I(k)* is the *k*-space interferogram, then it can be expressed as follows if a reflector as the sample,

$$I(k) = e^{j\Delta z k + jD(k)} \tag{5}$$

where Δz is the length difference between the reference mirror and the single sample reflector, and *D(k)* is the dispersion term. Further assume that such interferogram is sampled in the detector pixel space (*n*-space, with *n* being the index of the detector pixels), then the mapping function from *n*-space to *k*-space can be expressed as,

$$k = \Phi(n) \tag{6}$$

wherein the mapping relation is unknown. The detected interferogram from the linear detectors can be expressed as

$$I(n) = e^{j\Delta z \Phi(n) + jD(\Phi(n))} \tag{7}$$

We interpolated the interferogram to increase the data length by a factor of 4, using Fourier domain zero padding for improving the resampling quality [33]. Utilizing the Hilbert transform, which is denoted as $\mathcal{H}(\bullet)$, the phase curve *P(n)* then can be extracted:

$$P(n) = arg(\mathcal{H}(I(n)) = \Delta z\ \Phi(n) + D(\Phi(n)) \tag{8}$$

In the experiment, we recorded the interferograms at two different path lengths, and thus two phase curves $P_1(n)$ and $P_2(n)$ (Figs. 4(a) and 4(b)), were obtained using Eq. (8). To eliminate the dispersion term $D(\Phi(n))$ while extracting the remapping vector $\Phi(n)$, these two phase curves were subtracted,

$$P_1(n) - P_2(n) = \Delta z_1 \Phi(n) - \Delta z_2 \Phi(n) \tag{9}$$

and thus, $\Phi(n)$ can be calculated:

$$\Phi(n) = \frac{P_1(n) - P_2(n)}{\Delta z_1 - \Delta z_2} \tag{10}$$

where $\Delta z_1 - \Delta z_2$ is a constant distance. As $\Phi(n)$ was a monotonic function, we can use $\Phi^{-1}(k)$ to map the detected *n*-space data to *k*-space via a reverse mapping. Fig. 4(c) shows the linearly sampled *k*-space interferograms through interpolation.

After the first step *k*-space remapping of the interferogram data, the second step is to compensate the dispersion term *D(k)* between the reference and sample arm optics. We extracted the phase curve *P(k)* from the remapped interferogram *I(k)*:

$$P(k) = arg(\mathcal{H}(I(k)) = \Delta z k + D(k) \tag{11}$$

Since *D(k)* can be regarded as the high order distortion that was added to the term $\Delta z k$, we performed linear regression to *P(k)*, and obtained $P_{lr}(k) = \Delta z k$. Hence, *D(k)* was obtained with $D(k) = P(k) - P_{lr}(k)$. To implement dispersion compensation, the *k*-space interferogram was then point-by-point multiplied with a compensation term $e^{-jD(k)}$ before retrieval of the depth profile [4].

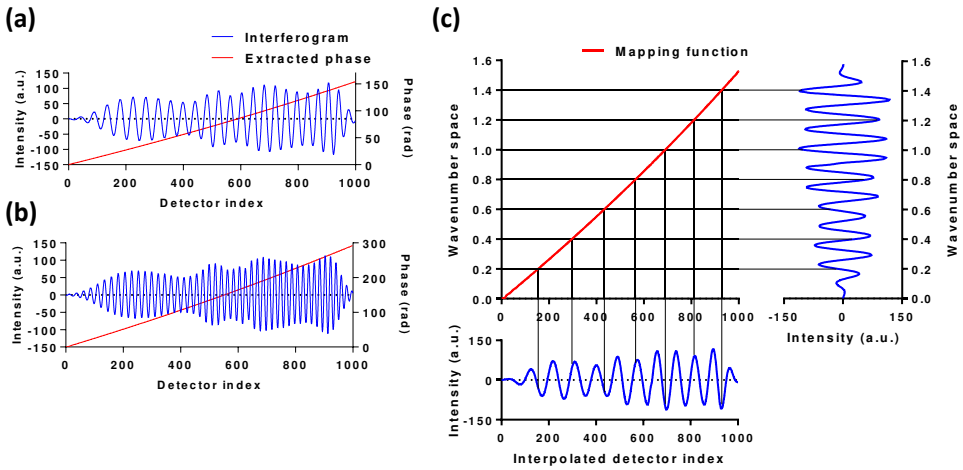

Fig. 4. Remapping of interferogram from the CCD detector space to the wavenumber space. (a-b) The spectral interferograms of a single reflective surface at two different optical paths Δz_1, Δz_2 between the reference and sample arms (blue line). The phase curve (red line) was extracted from the interferogram curve. (c) The remapping process from the CCD detector space to the wavenumber space using a calculated mapping function. The mapping function was obtained by point-by-point subtraction of the two phase curves in (a) and (b). The subtraction process could eliminate the unbalanced dispersion of the reference arm and the sample arm.

It is worth mentioning that in the above proposed algorithm, the influences of all factors, such as *k*-space nonlinearity, unbalanced dispersion of the reference and sample arm optics, aberration of both camera lens and the objective lens, etc., were taken into account for dispersion compensation. With such an algorithm, we were able to compensate the dispersion between the sample and the reference arm optics. Specifically, since this method calculates the mapping function using measured calibration data, but not the physical model of the spectrometer [33], it can be easily adopted in other OCT systems for dispersion correction purpose.

3. Results

To verify the feasibility of the SEES technique to HR-OCT imaging, we built a HRES-OCT and characterized its spatial resolutions first, and then tested it with biological tissue imaging; we also compared the results obtained by HRES-OCT with those obtained using an equivalent point source OCT. To build the point-source system, the sample optics of the HRES-OCT as shown in Fig. 1 was replaced by that in Fig. 1(a), wherein the prism was removed. However, the light source, spectrometer settings, illumination beam diameter, and objective lens were all the same as those of the HRES-OCT.

3.1 Spatial resolutions

In the equivalent point-source SD-OCT system, since the mode field diameter of the input single mode fiber (850 nm for P3-780A-FC-2, Thorlabs Inc.) was 4.5~5.5 μm and the magnification of the sample arm optics was (1/1.6X), the diffraction limited spot size at FWHM of such a system was predicted to be 4.3~5.2 μm at the focal plane.

To measure the transverse resolving capability of the HRES-OCT, we acquired a 3D image of the USAF resolution target. The actual scanning area was 0.98 mm × 0.98 mm, covering 512 pixels × 512 pixels. In the *en face* view (Fig. 5(a)), the vertical direction (Y) was along the spectrally extended line field, and therefore, in Fig. 5(a), the patterns along the vertical direction demonstrated the transverse resolving capability of the point-source system while the horizontal (X) patterns demonstrated that of the HRES-OCT system.

Fig. 5(b) depicts the averaged cross-sectional profiles for both vertical and horizontal line patterns of element 6 in group 6, which is marked by the yellow box as shown in Fig. 5(a). Results demonstrated that the 4.39 µm standard line-spacing between these line patterns could be clearly resolved, which matched well with the predicted value. The averaged line-pattern profiles shown in Fig. 5(b) demonstrate that the transverse resolving capability of HRES-OCT is slightly degraded when compared with the point-source OCT system (red curve vs. blue curve).

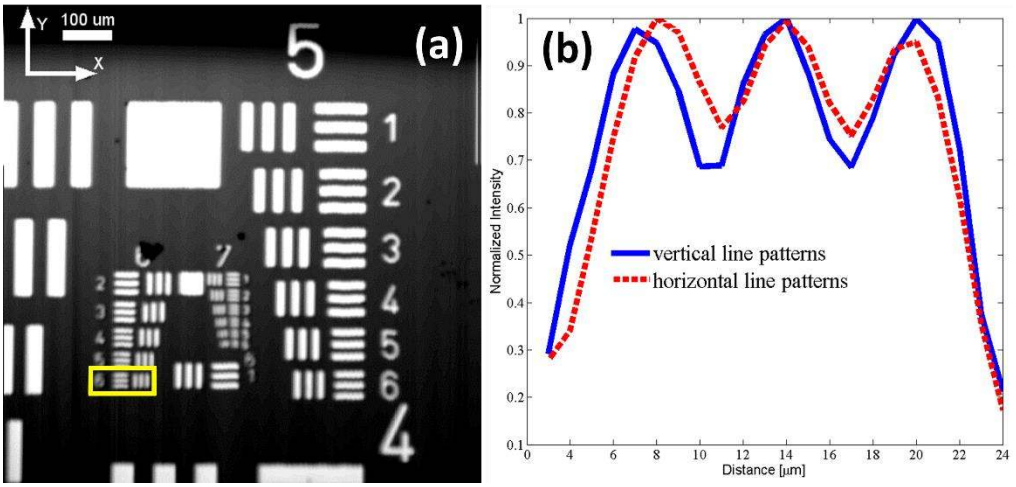

Fig. 5. Transverse resolution of HRES-OCT vs the point-source OCT system. (a) An *en face* 3D-image of the USAF 1951 resolution target acquired using HRES-OCT. (b) Cross-section profiles of the horizontal and vertical bars of group 6, element 6. Blue-solid line: cross-sectional profile of vertical bars; red-dashed lines: cross-sectional profile of the horizontal bars. Blue line represents the resolution power of the point source system, while red-line represents that of the HRES-OCT.

With the broadband SLD light source, the theoretical axial resolutions were calculated to be Δz = 1.93 µm in air for both HRES-OCT and the point-source OCT. To characterize its practical axial resolution, we measured the A-line profiles by placing a neutral density filter (NDF: NDL-10C-4, Thorlabs Inc.) with an attenuation of -49.2 dB in the sample arm optics and a mirror (PF10-03-P01, Thorlabs Inc.) at the sample plane. The measured axial resolution was tested to be 2.1 µm in air (Fig. 6), which was slightly lower than the theoretical value. Results also showed that the point spread functions (PSFs) of both systems coincided with each other well with a difference <5% at FWHM.

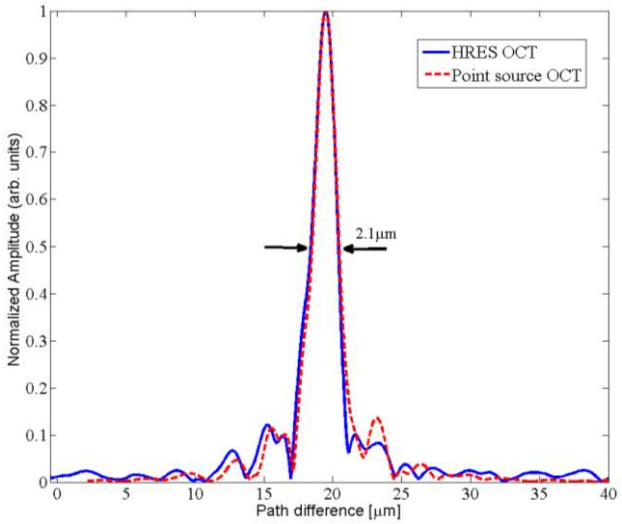

Fig. 6. Measured axial PSF of the HRES-OCT as compared with that of the point-source OCT system. Blue-solid line: PSF of the HRES-OCT; red-dashed line: PSF of the point-source OCT.

3.2 Sensitivity

To measure the sensitivity of the HRES-OCT, we placed a silver mirror (PF10-03-P01, Thorlabs Inc.) at the focal plane together with an NDF (NDL-10C-4, Thorlabs Inc.) at the sample arm optics. The total attenuation of such an NDF was measured to be -49.6 dB. We measured the signal to noise ratio (SNR) for an A-line signal. The SNR was measured to be 55.4 dB when the path difference between the two arms was 120 μm. Hence, the sensitivity of HRES-OCT system was estimated to be 105.0 dB, which agreed well with the theoretical value of 106.3 dB as calculated in Section 2.

Experiments were also carried out to characterize the imaging performance of HRES-OCT in the axial region. With an NDF filter (with total attenuation of 36.4 dB for both HRES-OCT and point-source system) inserted into the sample arm optics and an uncoated BK7 reflector (with an attenuation of 14 dB) used as a sample, we changed the path length of the reference arm optics and measured the intensity of an A-line signal at different reference arm distances. The measured intensity values at different distances were then normalized to that of the same A-line signal at ~4 μm distance. Figure 7 depicts the normalized signal intensity (in decibels) versus path-distance for HRES-OCT. As can be seen, the 6 dB sensitivity roll-off happens at ~1.1 mm for HRES-OCT system.

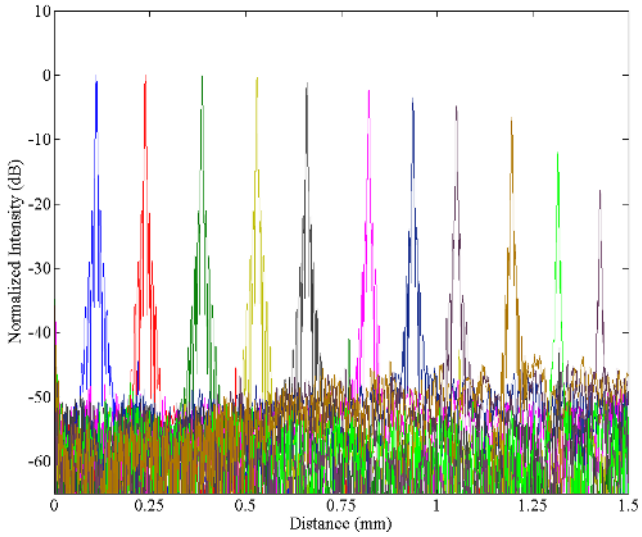

Fig. 7. The axial PSFs of an A-line signal at the different path-lengths of the reference arm optics for HRES-OCT.

3.3 Penetration depth

To verify the feasibility of the SEES technique for penetration depth improvement in high-resolution system, we imaged the human skin at the fingertip in vivo. Figure 8 depicts the ventral portion of a male volunteer's finger acquired by the point-source OCT and HRES-OCT, respectively. Fig. 8(a) shows the image obtained with the point-source OCT, and Fig. 8(b) is the image acquired by the HRES-OCT. Both images consist of 700 axial and 512 transverse pixels covering a range of 0.68 mm × 2.8 mm, and they were acquired at a frame rate of 20 frames per second (fps), with the focal point of the objective lens positioned at the middle of the depth range. The illumination power on the tissue was set to be 4.8 mW and 1.2 mW for HRES-OCT and the point source OCT, respectively. Results show that for both systems, the detailed skin structures, such as epidermis, sweat ducts, dermis, etc., can be clearly observed; while in the axial direction, however, HRES-OCT achieves higher imaging depth, especially for the epidermis and dermis layers, as compared with its point-source counterpart. Such depth enhancement with HRES-OCT can be easily understood: when tissue with the same backscattering coefficients is utilized for both the system, the one with higher illumination power (4.8 mW vs. 1.2 mW) achieves a higher SNR value, which thus leads to a higher penetration depth in the fingertip tissue.

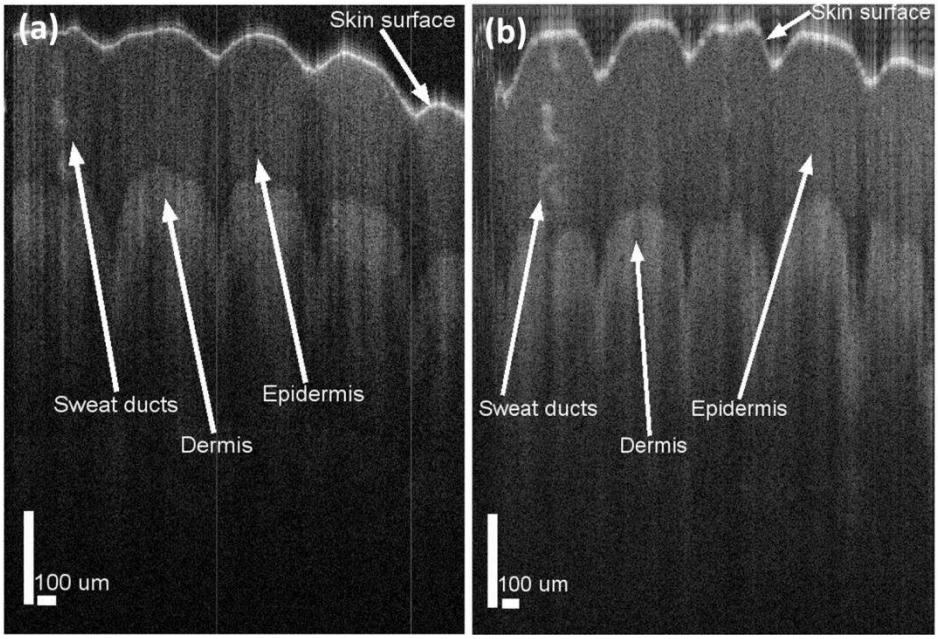

Fig. 8. Cross-sectional images of the human fingertip acquired *in vivo* at a frame rate of 20 fps with point source OCT and HRES-OCT, respectively. Both images consist of 700 axial × 512 transverse pixels, covering an area of 0.68 mm × 2.8 mm. (a) Image acquired by the point-source OCT system with illumination power of 1.2mW. (b) Image acquired using HRES-OCT with illumination power of 4.8mW.

To test the system's capability of suppressing the motion artifacts, we improved the A-line rate of HRES-OCT from 10K Hz (20 fps) to a maximum rate of 60K Hz (117 fps) and acquired images of the same area of the human fingertip *in vivo*. The illumination power on the sample was also set to be 4.8 mW. Fig. 9(a) depicts the image acquired using HRES-OCT at 60K Hz A-line rate. When comparing such image with the one acquired using the point-source system at 10K Hz (Fig. 9(b)), results demonstrate that the imaging depth of HRES-OCT at 60K Hz was still comparable to that of the point-source OCT at 10K Hz, and all the detailed skin structures could be observed clearly. Such result also prove that the imaging performance of HRES-OCT is acceptable at 60K Hz; when comparing to that of the point source system operating at 60K Hz A-line rate, such results in Fig. 9(a) should be even better as the sensitivity would drop with 60K Hz rate.

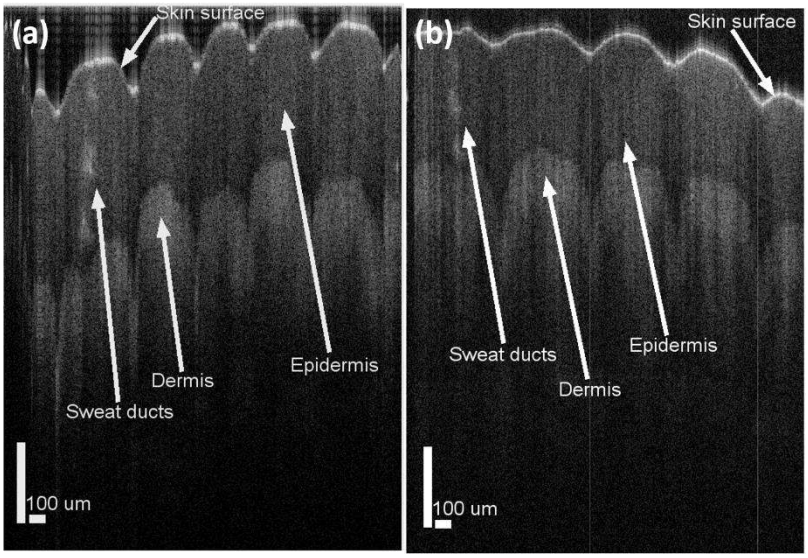

Fig. 9. Cross-sectional images of the human fingertip acquired *in vivo* at different A-line rate with HRES-OCT and the point source OCT, respectively. Both images consist of 700 axial × 512 transverse pixels, covering an area of 0.68 mm × 2.8 mm. (a) Image acquired using HRES-OCT with illumination power of 4.8mW at an A-line rate of 60K Hz (117 fps). (b) Image acquired by the point-source OCT system with illumination power of 1.2mW at an A-line rate of 60K Hz (20 fps).

To further verify the potential of the SEES technique in ophthalmic imaging, the swine optic nerve head (ONH) images were also acquired *ex vivo* using HRES-OCT and compared with those acquired by the point-source OCT. Fresh swine eyes were enucleated and dissected to expose the ONHs to the focused beam spot. All images were acquired at a frame rate of 20 fps, with each consisting of 512 A-lines. The galvo scanners' amplitude was configured to cover a 3D volume of 4.2 mm × 2.8 mm × 0.59 mm in x, y, z directions, respectively.

Assuming that the MPE for the point-source system was 0.7 mW, we set the illumination power of the point source system to be 0.7 mW and that of the HRES-OCT to be 2.8 mW. Results show that the ONH micro-structures, such as, sclera, pre-lamina (PL) and lamina cribrosa (LC) region, etc., can be seen clearly for both systems (Figs. 10(a-b)). However, the image acquired with HRES-OCT (Fig. 10(a)) provides more structure information of the LC region when compared with the point source OCT (Fig. 10(b)). This is due to the fact that the penetration depth of HRES-OCT is improved with the SEES technique. Figure 10(c) shows the same tissue image obtained by the point source system with an illumination power of 2.8 mW, which exceeds the MPE according to the clinical regulations. As can be seen, the penetration depth and the image quality of HRES-OCT (Fig. 10(a)) are comparable to those of the high power point source OCT, yet with an illumination power that is lower than the MPE under the safety regulation.

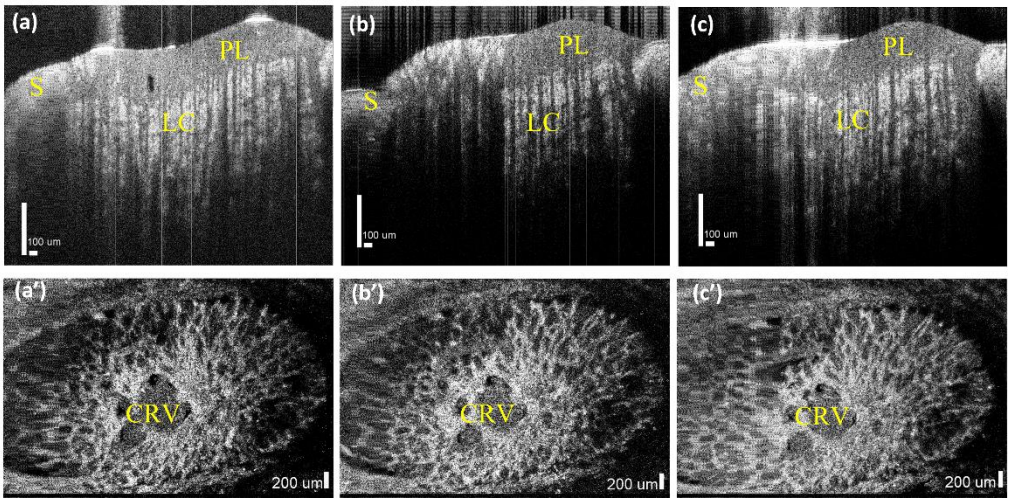

Fig. 10. Cross-sectional and *en face* images of the swine optic nerve head (ONH) acquired with HRES-OCT and point-source OCT *ex vivo.* (a) Image acquired by HRES-OCT with a sample power of 2.8 mW. (b) Image acquired by point-source OCT with a sample power of 0.7 mW. (c) Image acquired by point-source OCT with a sample power of 2.8 mW. (a'-c') the corresponding *en face* images of the swine ONH tissue. S: sclera; PL: pre-lamina; LC: lamina cribrosa; CRV: central retinal vessels.

4. Discussion and conclusion

The HRES-OCT helps visualize deeper tissue structures that are not readily visualized with the current point source system, such as lamina cribrosa and sclera. In addition, since the dispersive prism is the only additional element of HRES-OCT, the SEES apparatus is of low cost and compatible with the existing point source OCT as an add-on function, and thus, the HRES-OCT imaging system can be quickly and conveniently switched between the extended source mode and the point source mode by selecting between the prism and a reflective mirror.

Due to the dispersion effect of the prism, however, the SEES technique requires accurate spectral remapping and is also more sensitive to motion artifacts as compared with its point source counterpart. To solve the first issue, two easy and efficient methods were proposed for system calibration and dispersion compensation, respectively. These two methods solved the issue very well, and the dispersion compensation method can also be applied in some other OCT systems for dispersion corrections. With the maximum scanning speed reaching up to 60K A-lines/s, the motion artifacts with HRES-OCT have also been largely alleviated. Specifically, since the full spectrum of a single A-scan should be obtained to retrieve an OCT image, while each A-scan of HRES-OCT contains a 112 A-lines' scanning margin that was introduced in the calibration process, the equivalent A-line acquisition time of HRES-OCT was calculated to be $112/(6\times10^4)$= 1.87 ms in this study. Such time is much shorter than the 10 ms time required for the *in vivo* full-field OCT reported in [25], and thus should be fast enough to acquire OCT images with satisfactory motion artifacts. It is of our future interest to shift the SEES technique to existing high-speed standard point-source OCT as an add/on function for sensitivity improvement. We are also interested in reconfiguring such system so that it can be utilized for human retinal imaging *in vivo*.

In conclusion, we have demonstrated a high-resolution extended source OCT, i.e., HRES-OCT, using the SEES technique. The applicability of the SEES technique to HR-OCT system as well as its effectiveness for sensitivity enhancement was demonstrated both numerically and experimentally. The penetration depth improvement with the SEES technique for HR-OCT imaging was also verified using biological tissues *in vivo* and *ex vivo*. We summarized

the novelties of this study as three-fold: first, it is the first time, to the best of our knowledge, for the dispersion effect to be utilized for sensitivity enhancement in an ultrahigh-resolution OCT system. Second, we presented an easy and efficient dispersion compensation mechanism for HRES-OCT dispersion correction. Third, the maximum scanning speed of HRES-OCT reaches up to 60K A-lines/s.

Acknowledgment

This research is supported in part by the Nanyang Technological University (Startup grant: Linbo Liu), National Research Foundation Singapore (NRF2013NRF-POC001-021 and NRF-CRP13-2014-05), National Medical Research Council Singapore (NMRC/CBRG/0036/2013), Ministry of Education Singapore (MOE2013-T2-2-107).